Fluid assessment in dialysis patients by point-of-care magnetic relaxometry

Lina A. Colucci[1,2,3], **Kristin M. Corapi**[4], **Matthew Li**[1,2,3], **Xavier Vela Parada**[4], **Andrew Allegretti**[4], **Herbert Y. Lin**[4], **Dennis A. Ausiello**[4], **Matthew S. Rosen**[5,6], **Michael J. Cima**[3,7,*]

[1]Harvard-MIT Division of Health Sciences and Technology, Cambridge, MA, 02139, USA

[2]Institute for Medical Engineering and Science, MIT, Cambridge, MA 02139

[3]Koch Institute for Integrative Cancer Research, Massachusetts Institute of Technology, Cambridge, MA, 02139, USA

[4]Division of Nephrology, Department of Medicine, Massachusetts General Hospital, Harvard Medical School, 165 Cambridge Street, Boston, Massachusetts 02114, USA

[5]A.A. Martinos Center for Biomedical Imaging, Massachusetts General Hospital, Boston, MA

[6]Dept. of Physics, Harvard University, Cambridge, MA

[7]Department of Materials Science and Engineering, Massachusetts Institute of Technology, Cambridge, MA, 02139, USA

Abstract

Magnetic resonance imaging (MRI) is a powerful diagnostic tool, but its use is restricted to the scanner suite. The experiments described here demonstrate that a portable nuclear magnetic resonance (NMR) sensor can assess individual fluid status changes at the bedside in a fraction of the time. Quantitative T2 measurements of the lower leg of end-stage renal disease (ESRD) patients immediately before and after dialysis were compared to those of euvolemic healthy controls using both a 0.28 T bedside single-voxel sensor and a 1.5 T clinical scanner. We find that the first sign of fluid overload is an expanded muscle extracellular fluid (ECF) space, a finding undetectable at this stage on physical exam. A decrease in muscle ECF upon fluid removal was similarly detectable with the bedside sensor. Bioimpedance results generally perform worse than MRI and comparably to the bedside NMR sensor. These findings suggest that bedside NMR measurements may be an important method to identify fluid overload early in ESRD patients and potentially other patient populations as well.

One Sentence Summary:

Portable NMR sensors enable quantitative diagnostic measurements about fluid status to be made at the patient bedside.

Introduction

End-stage renal disease (ESRD) is associated with shortened life expectancy, despite intensive treatments such as hemodialysis (HD) (1, 2). The kidneys play an integral role in maintaining euvolemia, and patients with ESRD, even those who undergo thrice weekly HD for the purposes of removing toxins and excess fluid, are often plagued by chronic volume overload (3).

Underestimates of the fluid removal target during HD leave patients with ESRD prone to chronic volume overload, hypertension, and heart failure (1, 4–6), whereas excessive fluid removal leads to hypotension, muscle cramping, and subclinical ischemia (4–6). Both scenarios are associated with morbidity and mortality (6). A primary goal of HD is to bring patients with ESRD to their dry weight, the weight at which their extracellular volume is optimized. Determining a patient's true dry weight, however, is challenging (6). There are no accurate, objective, and noninvasive methods to monitor fluid status and determine whether a patient's extracellular volume is physiologic (5, 7, 8). The gold standard method includes a combination of subjective measurements, such as estimating the degree of lower-extremity edema (swelling) through palpation, and measurements subject to confounding, such as body weight change (5, 9–11). Nephrologists need better methods to monitor the volume status of their patients and inform their dialysis prescriptions.

A quantitative sensor to detect volume overload would benefit patient populations beyond simply those with ESRD. More than 6 million patients in the United States suffer from acute (sepsis or postsurgical) or chronic (congestive heart failure) fluid overload (12–14). Managing hypervolemia and its complications costs the U.S. health care system more than $35 billion annually (3, 15, 16).

Bioimpedance (BI) is a noninvasive technology used for fluid assessment. BI uses skin surface electrodes to deliver multifrequency, low current into the body (17, 18). The more fluid that is present, the less resistance the current encounters when traversing the body (18). The challenge for BI is that many factors, such as body geometry and skin properties, also affect resistance (5, 19). BI accounts for these multiple factors by developing population-specific equations to correlate the measured resistance (and reactance) to fluid volumes. One of the limitations of BI is that it does not work well when applied to patients outside of the population on which the predictive algorithms were developed (20).

Nuclear magnetic resonance (NMR) relaxometry, on the other hand, provides a direct, noninvasive measurement of fluid volume and its environment (21). Quantitative magnetic resonance imaging (MRI) relaxometry is more reliable than BI when measuring muscle hydration; however, it is impractical for routine use because MRI has limited availability and is restricted to use within the scanner suite (22). Portable NMR sensors can perform the

same quantitative measurements as MRI scanners while also being convenient for routine use. A variety of portable NMR sensor designs exist, many of which are single sided (also known as unilateral, strayfield, or inside-out NMR), which enables the magnet to be placed on the surface of the sample instead of surrounding it (23). Single-sided designs allow the sensor to be smaller than it would otherwise have to be to accommodate large samples. Portable NMR sensors are also often nonimaging, they are designed to take quantitative NMR relaxometry measurements of a bulk sample rather than thin, slice-wise measurements. Nonimaging NMR sensors have long been used in oil well logging (24, 25), food quality control (26), and airport security (27). Single-sided sensors have more recently been used in quantifying properties of biological tissues such as skin, tendon, and breast tissue (23, 28).

Inspired by the broad success of NMR sensors operating at low magnetic field, we demonstrate that a portable, nonimaging, single-sided NMR sensor can rapidly assess clinically relevant changes in the fluid status of hypervolemic patients with ESRD and differentiate them from euvolemic healthy controls with stable volume status. We validate this finding by using quantitative MRI measurements and compare it to the performance of a U.S. Food and Drug Administration (FDA)–approved BI device.

Results

Clinical study measuring participants at different fluid states

Seven patients with ESRD treated with chronic, thrice weekly HD and seven healthy control (HC) participants were enrolled into the study according to Institutional Review Board (IRB) guidelines, including written, informed consent. All enrolled HD participants were fluid overloaded, made apparent from clinical records of weight gain above their dry weight and the successful removal of fluid during their observed HD (used interchangeably in this text with dialysis) treatment. As is routine for dialysis treatments, ultrafiltration volume was informed by the change in weight from their target dry weight.

HD participants were measured before and after a single dialysis session, which allowed for a paired assessment of each participant at both a baseline state of hypervolemia and a later state closer to euvolemia after fluid removal. HC participants were subjected to the same clinical environment as HD participants: They sat in the same type of hospital bed for 4 hours, the length of a typical dialysis session, in the same hospital. It was assumed that HC participants would maintain a stable volume status throughout the study. Transverse proton NMR relaxation time (T_2) measurements were taken at the lower leg in all participants using both a 1.5-T MRI and a 0.28-T single-voxel, single-sided NMR sensor at the beginning and end of the study visit. BI measurements, weight, and blood draws were also taken at the same two time points (detailed in the "Study design" section of Materials and Methods). The demographics of the study cohort are summarized in Table 1, and participant-level data are detailed in table S1.

Tissue changes in response to dialysis by MRI

Quantitative T_2 MRI scans acquired at 1.5 T were used to determine which tissues and parameters (if any) changed in response to dialysis. Regions of interest (ROIs) were drawn in the MRI images to select distinct tissue groups (Fig. 1, A and B). The T_2 magnetization versus time [$M(t)$] data of each pixel was fit to an exponential decay model determined by the extra sum-ofsquares F test (table S2 and fig. S1). The optimal model was a biexponential decay for all tissues, except for bone, whose optimal model was monoexponential. The monoexponential model is a two-parameter fit, which produces an amplitude and relaxation time (A_{1-exp}, $T_{2,1-exp}$). The biexponential model is a four-parameter fit, which produces amplitudes and relaxation times for the short and long time components (A_{short}, $T_{2,short}$, A_{long}, $T_{2,long}$). The short component (A_{short}, $T_{2,short}$) of the biexponential fit of the muscle relates to intracellular fluid (ICF), whereas the long component (A_{long}, $T_{2,long}$) relates to extracellular fluid (ECF) (29–32)

$$M(t)_{1exp} = A_M e^{-\frac{t}{\tau_M}}$$

$$M(t)_{2exp} = A_S e^{-\frac{t}{\tau_S}} + A_L e^{\frac{t}{\tau_L}}$$

T_2 relaxation time is a measure of the molecular environment of hydrogen atoms. A sample that is in a more liquid state (free fluids, ascites, and edema) has a longer relaxation time. A sample that has restricted mobility (cellular water bound to macromolecules) has a short relaxation time. Amplitude is a measure of the number of protons in a particular molecular environment. Relative amplitude (RA) measures the quantity of hydrogen atoms in a particular environment compared to the quantity of hydrogen atoms in all other measured environments. The RA of the long component, RA_{long} (related to the relative amount of ECF), for example, is calculated by

$$R_L = \frac{A_L}{A_S + A_L} \times 100\%$$

Figure 1C shows the pixel-wise $T_{2,short}$ and $T_{2,long}$ for muscle and subcutaneous tissue for a representative participant (fig. S2 shows this histogram for all participants). The $T_{2,short}$ values are similar in the two tissues, whereas the $T_{2,long}$ values differ with the subcutaneous compartment having the longer $T_{2,long}$. The change from pre- to post-measurement was calculated for each parameter ($T_{2,short}$, $T_{2,long}$, RA_{long}) in each tissue type (Fig. 1, D to F, corresponding statistics in table S3, and corresponding histograms in figs. S3 to S6). The muscle, muscle subgroups, and whole leg (which consists primarily of muscle) are the only tissues to display statistically significant changes, primarily in RA_{long}, in response to dialysis. RA_{long} changes by 1 to 7% across various tissues in the leg. It is possible to calculate the expected change in total body water (TBW) based on the amount of fluid removed from each participant, their baseline body weight, and the fact that the body is composed of about 60% water (6, 33). The amount of fluid removed is calculated on the

basis of a participant's weight loss during the 4-hour period of dialysis/bed rest. Because the weight changes are acute, it is presumed that the reason for weight change is fluid loss rather than changes in body composition.

Expected % change in body water=fluid loss (kg)0.6*baseline body weight (kg)×100% From this calculation, we expected to see $1.2 \pm 0.5\%$ (min, 0.8%; max, 2.2%) body water changes in HC participants and $4.3 \pm 2.6\%$ (min, 1.1%; max, 8.9%) body water changes in HD participants (Table 1 and table S1), which is consistent with the reported change in RA_{long} values in Fig. 1F. We did not expect the RA_{long} values to perfectly match because changes in ECF may not directly track TBW changes and certainly not in specific tissues.

MRI: T_2 relaxation times

The change in pixel-wise T_2 relaxation times was compared between HC and HD participants across each ROI (Fig. 1, D and E, and table S3). Although the change in the short relaxation time achieved statistical significance in some muscle groups, the size of these changes was small (<5 ms), which does not make it an ideal indicator and is of little diagnostic consequence because relaxation time measurements typically have a precision of a few milliseconds. Long relaxation times, $T_{2,long}$, did not have any statistically significant changes anywhere in the leg when comparing average HC and HD participant values.

Upon individual inspection, three participants were found to have quantifiably elevated $T_{2,long}$ values: HD1, HD1b, and HD2b. A cumulative distribution function (cdf) plot of $T_{2,long}$ in the whole leg shows that these three participants had relaxation times that were greater than the 95% confidence interval of all participants (Fig. 2A). HD1, HD1b, and HD2b had among the highest concentrations of serum brain natriuretic peptide (BNP), a blood biomarker for volume overload (Fig. 2B). HD2b and HD1 had perifascial fluid deposits and subcutaneous edema visible on the MRI scans (although not detected on physical exam), which are precursors to pitting edema and can be seen in Fig. 2C as elevated relaxation time values bordering the leg.

MRI: Relative amplitudes

At baseline, most of the hypervolemic HD participants had elevated long RAs, RA_{long}, within the muscle compared to euvolemic HC participants (Fig. 2D and individual participant curves are plotted in fig. S7). An elevated RA_{long} value suggests that the ECF space of the tissue is expanded. The average RA_{long} for HD participants was significantly higher ($P < 0.01$) than that of HC participants at every percentile at baseline, which is expected because HD participants are hypervolemic and HC participants are euvolemic at baseline (table S4). The relative size of the ECF space, RA_{long}, of the muscle of HD participants decreased in response to dialysis such that their RA_{long} values were closer to those of euvolemic HC participants (Fig. 2, E and F, corresponding statistics in table S4). One of the main objectives of dialysis is to reduce excess ECF so that a patient reaches a euvolemic state (6).

The fitting of relaxivity data can also be performed on entire ROIs, which is a type of analysis similar to that of single-voxel NMR sensors rather than on individual pixels. Figure 3A shows the RA_{long} of the muscle ROI before and after dialysis; Fig. 3B shows the same

data in boxplot form (participant-level data presented in table S5). The average muscle RA_{long} value for hypervolemic HD participants was 28.1%, whereas that of euvolemic HCs was 16.5%, with a statistically significant difference of $P = 0.0025$ between the groups (table S5). Figure 3C shows the change in RA_{long} before and after dialysis for the HD and HC groups. No significant change in RA_{long} occurred with HC participants ($P = 0.7499$), but the RA_{long} value for HD participants decreased by an average of 3.9% ($P = 0.0157$) (table S5). HC participants did not experience substantial changes in fluid status, whereas HD participants had a recorded volume of fluid removed.

These observations were statistically significant on the average; closer inspection at the individual participant-level data reveals some interesting detail. There were two HC participants—HC 2 and HC 6—that, similar to HD participants, experienced a decrease in RA_{long} of the muscular tissue (Figs. 2F and 3A). We hypothesize that these two participants became dehydrated over the course of the study, as supported by their baseline blood values and subsequent intake and output (table S1). This hypothesis is consistent with our previous animal dehydration experiments, which showed the same pattern of RA decrease exclusively in the muscular tissue during acute dehydration (34). Furthermore, literature shows that nonexercisebased dehydration leads to a decrease primarily in the ECF of the muscle (35, 36).

Portable NMR sensor for bedside relaxometry measurements

Our laboratory has developed a nonimaging, single-sided, single-voxel NMR sensor that can be placed against most external soft-tissue parts of the anatomy (Fig. 4A; see additional sensor details in the "NMR sensor: Hardware" section of Materials and Methods) (37). The magnet has a 0.28-T main magnetic field (B_o) created by a unilateral Halbach magnet array (Fig. 4, B to E). The NMR sensor can collect 8000 data points along its T_2 decay curve measurement compared to only 32 points in the MRI measurement, which enables the NMR sensor data to be fit by a greater number of exponentials. Table S6 compares the specifications of a traditional MRI to those of our NMR sensor.

To understand how results from the two sensors compare to each other, we took back-to-back T_2 relaxation measurements of six phantom and ex vivo tissue samples with the same MRI, NMR sensor, and pulse sequences as in human measurements (fig. S8). The phantoms and ex vivo tissues spanned the T_2 relaxation time range that is found in the leg. The NMR and MRI T_2 relaxation time measurements had a linear correlation of $r^2 = 0.966$ (Fig. 5 and raw values are plotted in fig. S9). The NMR sensor relaxation time measurements were within 10% and within 8 ms of the MRI measurements across all sample types except for the liquid copper sulfate measurement (table S7). The NMR sensor has a relatively nonuniform magnetic field compared to the MRI. T_2 measurements taken with a Carr-Purcell-Meiboom-Gill (CPMG) pulse sequence, as is our protocol, are affected by field gradient, interecho spacing, and the sample's diffusivity (24, 38). The larger any of these parameters, the greater the reduction of the measured T_2 relaxation time. The aqueous copper sulfate phantom has the largest diffusivity of any of the samples and therefore the worst correspondence between MRI and NMR sensor. Also, as expected, the aqueous copper sulfate's NMR sensor T_2 value is lower than its MRI T_2 value. The water diffusivities within tissues are not as large as

those of liquid, with the exception of pockets of frank fluid accumulation. Therefore, good correspondence between our in vivo MRI and NMR sensor results was expected.

Bedside NMR measurements

We used the custom NMR sensor to take single-voxel T_2 measurements of the same location (lateral aspect of lower leg; Fig. 4E) at the same time points as the MRI measurements. The NMR sensor's measurement voxel contained subcutaneous tissue and muscular tissue. The MRI pixel-wise results provided a model with which to analyze a voxel containing these tissues. Both subcutaneous and muscular tissues contain two components (a component is an amplitude and relaxation time pair) as determined by the F test. The short component, which corresponds to ICF, has a relaxation time $T_{2,\text{short}}$ that overlaps for both tissues. The long component, which relates to ECF, has a relaxation time $T_{2,\text{long}}$ that does not overlap between the muscle and subcutaneous tissue (Fig. 1C). A voxel containing both subcutaneous and muscular tissue, therefore, should consist of three distinct relaxation times. Advised by the anatomical model and measured correspondence between the relaxation times of the MRI and NMR sensor described above, these MRI results were used to develop a three-exponential model for the NMR sensor data

$$M(t)_{3\exp} = A_1 e^{-\frac{t}{\tau_1}} + A_2 e^{-\frac{t}{\tau_2}} + A_3 e^{-\frac{t}{\tau_3}}$$

where we define the relative magnitude of the relaxation times as $T_{2,\text{a}} < T_{2,\text{b}} < T_{2,\text{c}}$. Similarly, the RA of the second relaxation peak, $T_{2,\text{b}}$, is given by

$$R_2 = \frac{A_2}{A_1 + A_2 + A_3} \times 100\%$$

In the MRI pixel-wise results, the first exponential, $T_{2,\text{a}}$, was consistently observed near 40 ms (Fig. 1C). The third exponential was observed between 200 and 250 ms. We therefore fixed $T_{2,\text{a}}$ and $T_{2,\text{c}}$ in the NMR sensor's three-exponential model to values of 40 and 250 ms. The middle component ($T_{2,\text{b}}$, A_b), which was expected to correspond to ECF of the muscular tissue, was allowed to float. Thus, the fitted parameters for each NMR sensor relixivity measurement were $T_{2,\text{b}}$, A_a (RA$_\text{a}$), A_b (RA$_\text{b}$), A_c (RA$_\text{c}$). The amplitude of the middle component (RA$_\text{b}$) was expected to decrease in response to dialysis.

The MRI data shown in Fig. 1C suggest that the middle relaxation time should be about 70 to 170 ms. The middle relaxation time, $T_{2,\text{b}}$, of the NMR sensor data was fit to within the expected range (80 to 130 ms). No trends were observed in the relaxation time data of the NMR sensor. The NMR sensor's RA$_\text{b}$ values, however, decreased significantly more in HD participants than in HC ones, just as was observed in the MRI data (Fig. 6A and table S8). This decrease corresponds to a reduction in the relative volume of ECF in the muscle. The relationship between the change in RA$_\text{b}$ and change in ECF resistance, R_e, as measured by leg segmental BI is shown in Fig. 6B ($r^2 = 0.477$).

The baseline RA$_\text{b}$ values were not statistically significantly different between HC and HD participants like they were when measured by MRI (Fig. 6C). This means that the NMR

sensor cannot differentiate between euvolemic and fluid-overloaded participants using a single measurement. We hypothesize that the worse performance of the NMR sensor compared to MRI arises from the fact that the constant-volume NMR sensor voxel includes variable ratios of subcutaneous tissue to muscle tissue. That ratio will be constant when comparing the pre- and post-measurement for a given patient but will vary between patients. This may be the reason that we achieve significance between HD and HC groups for RA_b pre-to-post changes but not RA_b pre- or post-values by themselves for the NMR sensor. This hypothesis is supported the fact that the amplitude of the third component, RA_c (which corresponds to subcutaneous tissue), and the thickness of subcutaneous tissue for each patient were correlated ($r^2 = 0.67$; Fig. 6D). A greater subcutaneous tissue thickness means that subcutaneous tissue occupies a greater portion of the sensor voxel.

We explored the minimum voxel size and location that a future NMR sensor would have to measure to distinguish euvolemia from volume overload using a single measurement. We drew several small ROIs in multiple different locations on the lower leg MRI scans (Fig. 6E). The average T_2 decay curve of each ROI was analyzed with biexponential decay curves. The results of the small ROIs are summarized in Fig. 6F (tables S9 to S12). A 0.5-cm^3 voxel (1 cm by 1 cm by 0.5 cm) within the anterior ($P = 0.0198$) or lateral ($P = 0.0091$) muscle groups was calculated to be sufficient to detect fluid-overloaded participants with a single measurement. If the 0.5-cm^3 voxel was split between muscle and subcutaneous tissue, however, then the measurement could not distinguish between euvolemic HC and hypervolemic HD participants. More muscle tissue must be measured to distinguish fluid overload from euvolemia with a single measurement. These results provide a minimum volume, penetration depth, and anatomical measurement location to inform future NMR sensor designs. The methods for designing a sensor that can meet these volume and penetration depth requirements have been outlined by Bashyam *et al.* (37).

BI measurements

BI, like the NMR sensor, could not typically distinguish between hypervolemic HD and euvolemic HC participants using a single measurement. The results obtained with raw BI resistance values—R_e and R_{inf}—are summarized in Fig. 7 (A to H), and tables S13 to S16. Only the whole-body R_e measurement could distinguish the two populations using a single measurement at baseline ($R_{e, whole body}$: $P = 0.0201$). None of the leg BI measurements could do so. On the other hand, none of the whole-body BI measurements could distinguish between the change in volume status that accompanies dialysis treatments versus the stable volume status of HC participants. Both segmental leg measurements could do so ($\Delta R_{e, leg}$: $P = 0.0383$, $\Delta R_{inf, leg}$: $P = 0.0023$). The ECF and TBW volumes obtained by inserting the raw BI resistance values into predictive equations are summarized in Fig. 7 (I to P). BI could not statistically significantly distinguish between euvolemic HC and hypervolemic HD participants when volume equations were applied across most measurement types, except for the ΔECF whole-body measurement (ΔECF whole body: $P = 0.027$).

Discussion:

Quantitative relaxometry—through both traditional MRI and nonimaging NMR sensors— can provide data about a patient's fluid status. Recruiting HD participants allowed us to study a hypervolemic population that became less hypervolemic at the end of the study, thereby allowing for paired analyses of the same person at two distinct fluid levels. HC participants were assumed to remain euvolemic throughout the study, although a few unexpected cases of dehydration were encountered. Even with our small sample size, we were able to differentiate between participants who were euvolemic or had varying degrees of volume overload (fig. S10). In addition, the MRI results seemed sensitive to participants who showed evidence of dehydration. None of the participants displayed clinical signs of volume overload on physical exam. Relaxometry metrics may be able to detect fluid overload before traditional clinical examination, which is the principle test used by physicians today.

The first sign of fluid overload in the lower leg region among the patients studied was an elevation in the RA_{long} in the muscle, which indicates an expanded relative ratio of ECF. Hypervolemic HD participants could be distinguished from euvolemic HC participants using a single MRI measurement of RA_{long} captured at a single time point. The two populations could also be distinguished via the MRI or NMR sensor's measurement of change in muscle RAlong and RA_b, respectively, which are related to a decrease in the relative ratio of muscle ECF. The observed changes in RA_{long} and RA_b values are within the expected range based on the percentage of fluid loss from study participants. An exploration of voxel sizes revealed that if a future NMR sensor can measure 0.5 cm^3 of the lateral or anterior lower leg muscles, then it should be able to distinguish euvolemic HC from hypervolemic HD participants based on a single measurement as well.

The $T_{2,long}$ of the lower leg among our most volume-overloaded patients was elevated, indicating that the molecular environment of the ECF space of these participants became more aqueous than normal. Previously published studies involving patients who were more volume overloaded than our patient population reported relaxation time increases in the lower leg as well (39, 40). To our knowledge, no studies have reported the RA_{long} increase that precedes relaxation time elevation.

We interpret these relaxometry findings with consideration of the physiologic mechanisms in place to regulate the distribution of salt and water. In the absence of kidney function (ESRD), nearly all salt and water intake is retained (save for small amounts lost via gastrointestinal and insensible excretion), which leads to expansion of the vascular space (41). The muscle's rich microvasculature network causes an initial predominance of interstitial fluid accumulation in the muscle as opposed to less vascular tissues. Eventually, the capacity of the muscle to hold excess water is exceeded, and lymphatic drainage is necessary. Lymphatic reabsorption occurs primarily in the subcutaneous tissue space, which is why perifascial fluid and subcutaneous edema are seen in more advanced cases of fluid overload (40). The removal of fluid via the vascular space, as in HD, leads to fluid removal in the same order as accumulation occurred, with well-vascularized muscle responding first.

One of the main objectives of HD is to reduce excess ECF volume (1, 5, 17, 22). Thus, the extent and location where those decreases occur can be quantified with MRI or, more economically, with a portable NMR sensor assuming that ECF volume scales with RA_{long} and RA_b, respectively. The observation that the RA_{long} of HD participants in the postdialysis measurement approaches the RA_{long} of HC participants matches the clinical observation that well-tolerated intradialytic fluid removal brings a hypervolemic patient closer to euvolemic status. We can speculate that the RA_{long} of HC participants represents something of a reference range for euvolemia, but further study is needed to explore this as a potential criterion for NMR-driven fluid removal during dialysis.

Furthermore, the amount of baseline hypervolemia typically encountered in maintenance HD patients represents the level of fluid overload for which it is most critical to have accurate clinical sensors. Clinicians do not need a sensor to determine that a patient with pitting edema, for example, is fluid overloaded. Clinicians would benefit, however, from a sensor that can detect the type of lower-level hypervolemia (<5 liters) in patients receiving chronic HD. Physical signs are typically not visible at this stage of hypervolemia, yet this level of fluid accumulation is nevertheless associated with increased morbidity and mortality (3, 6, 42).

HD consists of both ultrafiltration and removal of waste. We expect filtration to affect the relaxation times rather than the RAs because relaxation time is a measure of molecular environment. Furthermore, urea—a compound that accumulates in the body of patients with ESRD—is a known T_2-shortening agent that diffuses through all fluid spaces in the body (43, 44). If levels of urea were affecting our relaxometry measurements, then we would expect the T_2 relaxation times to be lower in HD participants than in HCs and then to increase after dialysis. In reality, T_2 relaxation times of HD participants were equal to or higher than those of HCs at all time points. Future studies will aim to fully decipher the role of these two processes by measuring HD patients that have pure filtration or pure fluid removal functions performed on them during dialysis, as well as by measuring nonuremic fluid–overloaded participants, such as patients with congestive heart failure with preserved renal function.

Our findings suggest that bedside NMR measurements may be a safe, noninvasive method to identify fluid overload and, therefore, inform therapy in patients with ESRD (guide dry weight determination) and potentially other patient populations (titrate diuretics in heart failure) to attain euvolemia with greater clinical efficacy. NMR has many benefits over other fluid-monitoring modalities. Continuous blood volume monitoring measures only relative blood volume changes, which can help reduce hypotensive episodes during dialysis but cannot tell whether a participant has attained their true dry weight or has residual fluid overload (5, 6, 17). BI is affected by factors like sweat, electrode placement, body shape assumptions, and the validity of population-specific equations, whereas NMR intrinsically measures signal from water molecules (5, 17, 45). In our head-to-head comparison of BI to magnetic resonance, BI measurements generally performed worse than MRI and comparably to the NMR sensor. The body resistance measured by a low-frequency current from wrist-to-ankle electrodes—$R_{e, whole\ body}$—was the only BI measurement that was able to statistically significantly distinguish between the HC and HD groups using a single baseline

measurement. Ironically, however, the statistical significance was lost when the raw R_e resistance values were inserted into an FDA-approved equation to estimate ECF volume in terms of liters. The BI device used is FDA-approved for estimating whole-body composition—including TBW and ECF—for healthy individuals with normal fluid physiologies. The loss of significance when converting from R_e to ECF volume likely comes from inserting data from dialysis patients into algorithms developed on euvolemic, healthy participants. The benefit of NMR over BI is that it inherently measures fluid volume (a benefit that is harnessed by the oil and food quality control industries) without relying on population-specific equations and assumptions about body shape.

One of the limitations of this study is that there were only 14 participants (7 in each group) due to the burden that the study design placed on dialysis patients, who are chronically ill. The HD participants had to travel to the study site, rather than their local dialysis unit, and bookended their dialysis treatment with an additional hour of imaging. We chose to obtain pre- and postdialysis measurements from each participant so that each participant could serve as his own control in an effort to mitigate the limited number of participants in the study. Another limitation is the fact that there may be other aspects of physiology (uremia and overall health) that make HC and HD participants different from one another other than simple fluid status. Larger future studies should expand to other patient populations to address these confounders.

The proof-of-concept in vivo NMR sensing for fluid status shown here is only one of the many possible use cases for point-of-care relaxometry. Many diagnostic use cases for quantitative NMR biomarkers already exist, such as monitoring progression of multiple sclerosis, assessing iron overload in the liver, and identifying inflammatory muscular disorders (46–48). Portable NMR sensors can make it economically feasible to bring these new diagnostic discoveries to the clinic and improve patient care.

Future NMR sensor designs are not limited to a single-sided design or even to permanent magnets. Future work should experiment with lower field strengths, different purpose-built magnet constructions (optimized for curved surfaces or greater penetration depths), and other parts of the anatomy (lung and abdomen) (49–53). The measurement of additional relaxometry parameters, like T_1, or taking two-dimensional measurements such as T_2-diffusion or T_1-T_2, will enable further probing into physiology. The results of this study lay the groundwork for the diagnostic potential of NMR measurements to be brought out of radiology suites to the patient bedside and, eventually, into the patient's home.

MATERIALS AND METHODS

Study design

The overall goal of the work was to study the relaxometry findings that accompany changes in fluid status using both a portable NMR sensor and traditional MRI. For each participant, contact began and ended with MRI scans and consisted of HD (for HD participants) or bed rest (for HC participants) in between the two scans. MRI scans were conducted at the Athinoula A. Martinos Center for Biomedical Imaging (Charlestown, MA) and dialysis/bed

rest was conducted at the Massachusetts General Hospital (MGH) Main Campus (Boston, MA) in either the Dialysis Unit or the Clinical Research Center.

HD participants received their usual HD treatment (3 to 4 hours) in a hospital bed (in a reclined supine position with legs outstretched). HC participants sat on the same type of hospital bed for 4 hours. All intake and output were recorded for each participant during this interval. The following set of measurements was taken at the start and end of the dialysis/bed rest period:

1. Standing weight measurement

2. Blood work

3. Portable NMR sensor measurements: T_2 measurements of the lower leg with the single-sided NMR sensor

4. BI measurements: whole-body (wrist-to-ankle electrode placement) and leg segmental (upper calf-to-lower calf electrode placement) measurements

   Protocols for each measurement are detailed in subsequent sections. All participants were given the option of a to-go snack before returning to the Martinos Center for the second MRI.

Patient population

Seven patients with ESRD maintained with chronic thrice weekly HD and seven HC participants were recruited. One HC participant and two HD participants completed the study twice (denoted by "b" in the participant ID of their second visit). Participants were recruited from the Partners HealthCare clinical study recruitment email list, from recommendations from nephrologists, or from previous participation in pilot studies (when agreed to be contacted again). Enrollment was limited to males over the age of 25 years with a body mass index (BMI) between 18.5 and 40. Patients were excluded if they had a pacemaker, metal implants, or severe anemia (Hgb < 7.5 mg/dl) or had a history of limb amputation. HC participants reported no history of renal disease, cardiac disease, or other chronic conditions. HD and HC participants were age-matched by decade. Basic demographics were recorded for all participants. The study was approved by the Partners Human Research Committee, which is Partners HealthCare's IRB (Partners approval no. 2015P000011), and written, informed consent was obtained from each participant.

Blood work

All participants had blood drawn at the beginning of the 4-hour study interval after the first MRI. Laboratory work included the following: serum sodium, blood urea nitrogen (BUN), creatinine, complete hemoglobin and hematocrit, serum osmolality, and B-type natriuretic peptide (proBNP). HD participants also had routine pre- and postdialysis laboratories as dictated by our hospital's dialysis unit protocols, and a sample of blood was collected for storage in a biorepository.

MRI scans

MRI scans of the lower leg (upper calf) were obtained on a 1.5-T Siemens Avanto Scanner (Siemens Medical Solutions, software version Syngo MR B17) and CP extremity coil at the Martinos Center (Charlestown, MA). The upper calf (right leg for HC participants; leg contralateral to dialysis access site for HD participants) was positioned at the center of the extremity coil using padding when necessary. A localizing capsule was placed on the lateral aspect of the widest part of the calf (MR-SPOT 121, Beekley Medical Corp.). An initial set of localizing MRI scans were performed to find the location of the capsule [scanning sequence/variant, GR/SP (fl2d1); repetition time TR = 7.7 ms; echo time TE = 3.28 ms; flip angle FA = 20°; slice thickness = 6 mm; three slices in each anatomical direction]. A quantitative multiecho spin echo T_2 scan (se2d32) was performed with parameters TR = 3300 ms, TE = 8 ms, 32 echoes, 1 average, 4 sagittal slices of 5-mm thickness with 60% spacing (3 mm) between slices, 192×144 matrix (75% phase field of view), 1×1–mm in-plane pixel resolution, and a total acquisition time of 7 min 53 s. The sagittal scans were positioned such that the localizing capsule appeared in every slice.

MRI analysis: Software

The raw digital imaging and communications in medicine (DICOM) images from the scanner were converted to Neuroimaging Informatics Technology Initiative (NIfTI) format with FreeSurfer software (Martinos Center, Charlestown, MA), ROIs were hand-drawn on each slice of each scan using FSLeyes (previously FSLview) (54), and all further analyses were performed in MATLAB 2017b (MathWorks Inc., Natick, MA). All processing scripts are available in the repository: https://github.com/lcolucci/portable-nmr.

The hand-drawn ROIs were as follows: (i) Subcutaneous tissue: includes skin, fat and blood vessels in the fat; (ii) Bone and marrow: both include tibia and fibula; (iii) Muscular tissue: includes muscle, fascia, nerves, and blood vessels; and (iv) Whole leg: includes all of the aforementioned tissues. The following muscle group ROIs were drawn on the first slice of each scan: gastrocnemius (includes both medial and lateral heads), soleus, deep posterior (includes flexor hallucis longus, tibialis posterior, and flexor digitorum longus), anterior (includes tibialis anterior, extensor halluces longus, and extensor digitorum longus), and lateral (includes peroneus brevis and peroneus longus).

MRI analysis: Pixel-wise

The quantitative T_2 MRI images were analyzed by fitting each pixel on each slice with a mono- and biexponential decay. An *F* test was used to determine the optimal model for pixels within each tissue type (table S2), which showed that a biexponential fit was optimal for all tissue types except for bone. The initial point of the T_2 decay was ignored because of lack of stimulated echo effects. There were a total of 31 points from 16 to 256 ms with 8 ms of spacing that were fit to the following equations

$$M(t)_{1\exp} = A_M e^{-\frac{t}{\tau_M}}$$

$$M(t)_{2\exp} = A_S e^{-\frac{t}{\tau_S}} + A_L e^{\frac{t}{\tau_L}}$$

The starting values used for the biexponential fit were (A_{short} = 1500, $T_{2,short}$ = 50, A_{long} = 1500, $T_{2,long}$ = 210). The upper and lower limits for the fittings were set to 10,000 and 0, respectively. A nonlinear least-squares fitting method with a trust-region algorithm was used to perform the fits using MATLAB 2017b.

Pixel fit results were deleted if any of the following criteria were met: (i) the root mean squared error (RMSE) of the pixel fit was greater than the 99th RMSE percentile for that scan, (ii) either of the two relaxation times was less than 0.5 TE = 4 ms, (iii) either of the two relaxation times was greater than the maximum T_2 that could be expected to be measured with less than 5% relative error [calculated by the empirically derived expression 25.63* signal-to-noise ratio (SNR) + 197.6], (iv) the 95% confidence interval of any parameter was fit to NaN, or (v) the difference between the two relaxation times was less than 10 ms. Figure S26 shows all pixels that were deleted because of these criteria.

The cdf plots of the pixel-wise data visually show the percentage of pixels that are below a particular value (for code, see the "Computer code for statistical tests: no. 5 cdf plots for pixel-wise MRI data" section of the Supplementary Materials; fig. S7) The pre-to-post change for pixel-wise data is calculated by first subtracting the pre- and post-cdfs from each other and then integrating across the difference cdf curve (Fig. 2F).

MRI analysis: ROI

All pixels within an ROI were averaged together to produce a single T_2 decay curve. A mono- or biexponential fit was then performed on the average 31-point (because the first point was ignored) decay for that ROI according to the same specifications described in the pixel-wise section above.

Subcutaneous thickness measurements

The subcutaneous tissue thicknesses for each participant were calculated from the MRI-localizing scans using the length measurement tool on the software program OsiriX Lite DICOM Viewer (Pixmeo SARL). The thickness of the subcutaneous tissue was measured in four locations around the localizing marker on each of the three sagittal localizer slices for both pre- and post-scans. All 24 subcutaneous thickness values were averaged together to obtain the average skin and subcutaneous thickness for a particular participant. The subcutaneous tissue thickness traversed by the NMR sensor is less than the values measured with this method. The subcutaneous tissue is compressed by a few millimeters during data collection when the leg is pressed against the hard surface of the NMR sensor.

NMR sensor: Clinical setup

The NMR sensor was attached to the platform of a custom aluminum cart that extended onto the patient's bed (Fig. 4D). The participant's pant leg was rolled up, and their lower leg was put directly on the aluminum platform for electrical grounding and directly against the

surface of the sensor coil (Fig. 4D). The cart position was adjusted such that the sensor coil was on the same spot as the MRI-localizing marker. This ensured that the NMR sensor measured the same anatomical location as the MRI. Participants were instructed not to move their leg for the duration of the NMR measurement, and data collection was restarted if patients moved.

Ambient and magnet temperatures were recorded throughout the dialysis session with a continuous temperature logger and K-type thermocouples (RDXL4SD, OMEGA Engineering). A phantom filled with an aqueous solution of copper sulfate of known T_2 relaxation time was taken with each human measurement so that any sensor malfunctions could be immediately identified. Ambient temperatures tended to rise throughout the study because of the body heat of the study participant and study staff sitting in a small hospital room. The measured T_2 of the phantom, however, did not change by more than 2.8 ms (an outlier that occurred once). The average pre-to-post change in measured phantom T_2 value was, in fact, much smaller at 0.84 ± 0.78 ms (table S17). This phantom validation step ensured that the sensor was functioning properly and measured consistent T_2 values throughout the study.

NMR sensor: Hardware

We developed a custom single-sided, sweet-spot NMR sensor for this study that can be placed against most external soft-tissue parts of the body. The magnet has a 0.28-T main magnetic field (B_0) created by a unilateral linear Halbach design (37). The magnetic field is created by 180 cuboidal neodymium iron boron (NdFeB, N52 grade) magnets (Viona Magnetics, New York, USA) positioned across five slabs in a 6×6 grid within each slab. Each magnet's magnetization orientation points in a different direction based on which slab it is in, as shown in Fig. 4, B and C. The sensor weighs about 4.9 kg and measures about 9 cm by 9 cm by 15 cm.

Our magnet's "sweet spot" region has a saddle shape where the B_0 field is about 80 mm^3 (4 mm by 5 mm by 4 mm) in volume at 0.28-T field strength (B_0 field map shown in fig. S12). The transmit-receive coil is a single circular solenoid coil about 1.6 cm in diameter tuned to 11.61 MHz. More about the sensor design can be read by Bashyam *et al.* (37). The custom magnet was connected to a Kea2 spectrometer with dual transmit channels at 1 to 100 MHz and a duplexer/preamplifier module operating from 7 to 16 MHz (Magritek, Ltd., Wellington, New Zealand and Aachen, Germany).

NMR sensor: Pulse sequences

Prospa software was used to run various pulse sequences (Magritek, Ltd., Wellington, New Zealand and Aachen, Germany). The T_2 measurements were taken using a CPMG pulse sequence with 8000 echoes, 65-μs echo time, 3 dummy echoes, 12-μs pulse length, 16 points per echo, 0.5-μs dwell time, 2000-kHz bandwidth, 800- to 3500-ms interexperimental delay, autophasing, 8 averages per measurement, and 11.61-Mz B_1 frequency. Hard 90° and 180° pulses were used (−12- and − 6-dB pulse attenuation, respectively), and phase cycling was performed. Eight averages were taken per measurement, and 3 to 10 measurements per time point were averaged together in the postprocessing analysis.

NMR sensor: Data analysis

The T_2 decays from each time point were averaged together using a straight-averaging technique. The first point was deleted from the averaged decay. The averaged decay is plotted in fig. S13 for a representative HC and HD participant. The average SNR of all participants across all time points is 80.4 ± 24.5 (mean ± SD). SNR was calculated as the ratio of the maximum value of T_2 decay curve divided by the SD of the noise floor at the end of the T_2 decay. The decay signal was fit to a three-exponential decay on the basis of the model developed through the MRI pixel-by-pixel results. The NMR sensor data were forced to fit to a three-exponential decay where the first exponential was fixed at 40 ms, the third exponential was fixed at 250 ms, and all other parameters were allowed to float.

$$M(t)_{3\mathrm{exp}} = A_1 e^{-\frac{t}{40ms}} + A_2 e^{-\frac{t}{\tau_2}} + A_3 e^{\frac{t}{250ms}}$$

The starting values used for the fit were ($A_a = 9$, $A_b = 5$, $A_c = 7$, $T_{2,b} = 100$). The lower and upper limits for the fittings were set to zero and infinity, respectively, for the amplitudes, and 0 and 250 for relaxation time 2. A nonlinear least-squares fitting method with a trust-region algorithm was used to perform the fits using MATLAB 2017b (MathWorks Inc., Natick, MA).

Phantoms and ex vivo tissues

Three phantoms—vegetable oil, agar, and an aqueous copper sulfate solution (CuSO4; Sigma-Aldrich, Missouri, USA)—and three ex vivo tissue samples—muscle (bovine), fat (porcine), and skin (porcine)—were measured with the MRI and NMR sensor protocols described above for human participants. The aqueous copper sulfate was diluted with deionized water to ensure a longer relaxation time. The ex vivo tissues were kept in a sealed petri dish to avoid dehydration over time. The agar-based phantom was made by the protocol in Hattori *et al.* (55).

BI: Setup

BI spectroscopy measurements were taken with an ImpediMed SFB7 unit and dual-tab body composition electrodes (ImpediMed, Ltd., Australia). The system uses a single-channel tetrapolar configuration and performs a frequency sweep of 256 frequencies from 10 to 500 kHz. The ImpediMed Bioimp software (version 5.4.0.3) was used to apply Cole analysis and Hanai mixture theory to the raw data. For whole-body BI measurements, the two dual-tab electrodes were placed at the wrist and ankle of the side of the body contralateral to the dialysis patient's access (right side for HCs). For the leg segmental BI measurements, the two dual-tab electrodes were placed at the lateral aspect of the lower leg at the same side of the body. The distance between the two leg electrodes and the lower leg length (from fibula head to the lateral malleolus) was recorded.

BI: Analysis

Three BI measurements were taken at the pre- and post-time points, and results were averaged together. If any of the resistance values fit by the model were zero, then the trial

was excluded from the average. The R_e (modeled zero-frequency resistance, correlated to ECF), R_{inf} (modeled infinite-frequency resistance, correlated to TBW), and whole-body TBW and ECF values were taken directly from the ImpediMed Bioimp software (FDA-approved for healthy, euvolemic individuals). The leg segmental TBW and ECF values were manually calculated on the basis of the following equations published in the Hydra Model 4200 Manual (56)

$$ECF = \frac{\rho_{ECF}^{2/3}}{3*(4\pi)^{1/3}*1000} * L * \left(C_1^2 + C_1^2 + C_1 C_2\right) * \left(\frac{L}{C_1 C_2 R_E}\right)^{2/3}$$

$$\left(1 + \frac{ICF}{ECF}\right)^{5/2} = \left(\frac{R_E + R_I}{R_I}\right)\left(1 + \frac{k_\rho ICF}{ECF}\right)$$

$$k_\rho = \frac{\rho_{ICF}}{\rho_{ECF}}$$

$$TBW = ECF + ICF$$

where ECF is the predicted segmental extracellular fluid volume (liter), ICF is the predicted segmental intracellular fluid volume (liter), ρ_{ECF} is the resistivity of the extracellular fluid (ohms·m) [273.9 ohms·m for males and 235.5 ohms·m for females (values provided by ImpediMed Inc.)], ρ_{ICF} is the resistivity of the intracellular fluid (ohms.m) [937.2 ohms.m for males and 894.2 ohms.m for females (values provided by ImpediMed Inc.)], L is the lower leg length (cm), C_1 is the lower leg circumference (cm), C_2 is the lower leg circumference (cm), R_e is the extracellular resistance value from the model fitting (ohms), and R_i is the intracellular resistance value from the model fitting (ohms).

The reported $ECF_{leg\ segmental}$ and $TBW_{leg\ segmental}$ values were calculated using lower leg length, rather than electrode spacing because electrode spacing was not recorded for participant HC3.

Statistical analyses

Statistical tests were calculated in MATLAB 2017b (MathWorks Inc., Natick, MA) and RStudio (RStudio Inc., Boston, MA). All tests were two sided, and $P < 0.05$ was considered statistically significant. All statistics presented in this paper fall into one of the following four categories. The MATLAB or R commands corresponding to each of these statistical tests are provided in the "Computer code used for statistical tests" section of the Supplementary Materials.

Comparison of HC and HD groups (two-sample).—The statistical significance between the HC and HD groups was compared using both a Welch test and a permutation

test. Using either P value does not change the conclusions presented in the paper. The permutation test is more appropriate given the small sample size ($n = 14$).

1. Welch test: two-sample, two-sided t test with unequal variances. The Satterthwaite's approximation was used to calculate the effective degrees of freedom.

2. Permutation test (two-sample): two-sample permutation test using Monte Carlo method with $10^5 - 1$ replications.

Comparison of a single group at two time points (paired).—When comparing the same participant group at two different time points (i.e., HCs pre versus HCs post), both a paired Student's t test and a one-sample permutation test (on the difference, i.e., diff = HC_{pre} − HC_{post}) were used. Using either P value does not change the conclusions presented in the paper. The permutation test is more appropriate given the small sample size ($n = 14$).

1. Permutation test (one-sample): Fisher's one-sample permutation, two-sided test with 10^5 permutations.

2. Paired t test: paired, two-sided Student's t test.

Quantile regression of pixel-wise MRI data.—A quantile regression with clustering was used on the pixel-wise MRI data to quantify the difference between HC and HD groups at each time point.

Quantile regression with clustering: quantile regression with wild bootstrap method proposed by Feng $et~al.$ (57) to estimate SEs because the data had clustered responses (i.e., each participant has data from many pixels, which are not independent).

Determination of optimal model for T$_2$ data fitting.—The extra sum-of-squares F test, or simply F test, was used to determine the optimal number of exponentials that should be used to model the T_2 data. The test compares two nested models where one model is a simpler version of the other. The relationship between the relative increase in sum of squares and relative increase in degrees of freedom is expressed as an F ratio

$$Sum~of~Squares = SS = \sum_{i=1}^{n} (y - y_i)^2$$

$$F~ratio = \frac{(SS1 - SS2)/SS2}{(DF1 - DF2)/DF2}$$

where y is the true value of the data, y_i is the value predicted by the model, and DF, or degrees of freedom, is defined as $n - m$ where n is the number of data points and m is the number of parameters in the model. The more complex model is defined as model 2 and the simpler model is model 1.

The *P* value is obtained from an *F* distribution look-up table. The null hypothesis is that the simpler model is correct. We set our *P* value threshold to 0.05.

Data and Code Availability

Code to run all analyses in this paper is available on https://github.com/lcolucci/MRI (*Note to reviewer: code will migrate to Zenodo before publication*). Data is available from the corresponding author upon reasonable request.

Supplementary Material

Refer to Web version on PubMed Central for supplementary material.

Acknowledgments:

REFERENCES AND NOTES

1. Siriopol D, Hogas S, Voroneanu L, Onofriescu M, Apetrii M, Oleniuc M, Moscalu M, Sascau R, Covic A, Predicting mortality in haemodialysis patients: A comparison between lung ultrasonography, bioimpedance data and echocardiography parameters. Nephrol. Dial. Transplant 28, 2851–2859 (2013). [PubMed: 23828163]

2. Zoccali C, Moissl U, Chazot C, Mallamaci F, Tripepi G, Arkossy O, Wabel P, Stuard S, Chronic Fluid Overload and Mortality in ESRD. J. Am. Soc. Nephrol 28, 2491–2497 (2017). [PubMed: 28473637]

3. Ekinci C, Karabork M, Siriopol D, Dincer N, Covic A, Kanbay M, Effects of volume overload and current techniques for the assessment of fluid status in patients with renal disease. Blood Purif. 46, 34–47 (2018). [PubMed: 29649794]

4. Reddan DN, Szczech LA, Hasselblad V, Lowrie EG, Lindsay RM, Himmelfarb J, Toto RD, Stivelman J, Winchester JF, Zillman LA, Califf RM, Owen WF, Intradialytic blood volume monitoring in ambulatory hemodialysis patients: a randomized trial. J. Am. Soc. Nephrol 16, 2162–2169 (2005). [PubMed: 15930095]

5. Ishibe S, Peixoto AJ, Methods of assessment of volume status and intercompartmental fluid shifts in hemodialysis patients: Implications in clinical practice. Semin. Dial 17, 37–43 (2004). [PubMed: 14717810]

6. Taal MW, Chertow GM, Marsden PA, Skorecki K, Yu ASL, Brenner BM, Brenner and Rector's The Kidney (Elsevier Health Sciences, 2011).

7. Armstrong LE, Assessing hydration status: The elusive gold standard. J. Am. Coll. Nutr 26, 575S–584S (2007). [PubMed: 17921468]

8. Sinha AD, Why assistive technology is needed for probing of dry weight. Blood Purif. 31, 197–202 (2011). [PubMed: 21228590]

9. Agarwal R, Weir MR, Dry-weight: A concept revisited in an effort to avoid medication-directed approaches for blood pressure control in hemodialysis patients. Clin. J. Am. Soc. Nephrol 5, 1255–1260 (2010).

10. Fallick C, Sobotka PA, Dunlap ME, Sympathetically mediated changes in capacitance: Redistribution of the venous reservoir as a cause of decompensation. Circ. Heart Fail 4, 669–675 (2011). [PubMed: 21934091]

11. Agarwal R, Volume overload in dialysis: The elephant in the room, no one can see. Am. J. Nephrol 38, 75–77 (2013). [PubMed: 23838679]

12. Jessup M, Brozena S, Heart Failure. N. Engl. J. Med 348, 2007–2018 (2003). [PubMed: 12748317]

13. Frank Peacock W, Soto KM, Current technique of fluid status assessment. Congest. Heart Fail 16, S45–S51 (2010). [PubMed: 20653711]

14. Walsh SR, Cook EJ, Bentley R, Farooq N, Gardner-Thorpe J, Tang T, Gaunt ME, Coveney EC, Perioperative fluid management: Prospective audit. Int. J. Clin. Pract 62, 492–497 (2008). [PubMed: 17537185]

15. Gheorghiade M, Filippatos G, De Luca L, Burnett J, Congestion in acute heart failure syndromes: An essential target of evaluation and treatment. Am. J. Med 119, S3–S10 (2006).

16. Sieck S, in Short Stay Management of Acute Heart Failure, Peacock WF, Ed. (Humana Press, Totowa, NJ, 2012), pp. 9–32.

17. Dou Y, Zhu F, Kotanko P, Assessment of extracellular fluid volume and fluid status in hemodialysis patients: current status and technical advances. Semin. Dial 25, 377–387 (2012). [PubMed: 22686593]

18. Kyle UG, Bosaeus I, De Lorenzo AD, Deurenberg P, Elia M, Gómez JM, Heitmann BL, Kent-Smith L, Melchior J-C, Pirlich M, Scharfetter H, Schols AMWJ, Pichard C, Bioelectrical impedance analysis—Part I: review of principles and methods. Clin. Nutr 23, 1226–1243 (2004). [PubMed: 15380917]

19. Zuo CS, Villafuerte RA, Henry ME, Dobbins RL, Lee C, Sung Y, Haws C, Butman M, Miller S, Manos A, Orban BS, Brown AP, Hodge R, Nunez DJ, Renshaw PF, MRI assessment of drug-induced fluid accumulation in humans: Validation of the technology. Magn. Reson. Imaging 26, 629–637 (2008). [PubMed: 18420368]

20. Dehghan M, Merchant AT, Is bioelectrical impedance accurate for use in large epidemiological studies? Nutr. J 7, 26 (2008). [PubMed: 18778488]

21. Mathur-De Vré R, The NMR studies of water in biological systems. Prog. Biophys. Mol. Biol 35, 103–134 (1979). [PubMed: 387052]

22. Sawant A, House AA, Chesworth BM, Gati J, Lindsay R, Connelly DM, Bartha R, Overend TJ, Reliability of calf bioelectrical impedance spectroscopy and magnetic-resonanceimaging-acquired skeletal muscle hydration measures in healthy people. Physiol. J 2013, 563494 (2013).

23. Casanova F, Perlo J, Blümich B, Single-Sided NMR (Springer, 2011).

24. Coates GR, Xiao L, Prammer MG, NMR Logging: Principles and Applications (Halliburton Energy Services Publication, 1999).

25. Allen D, Crary S, Freedman R, Andreani M, Klopf W, Badry R, Flaum C, Kenyon W, Kleinberg R, Gossenberg P, Horkowitz J, Logan D, Singer J, White J, How to use borehole nuclear magnetic resonance. Oilf. Rev. Summer, 34–57 (1997).

26. Todt H, Guthausen G, Burk W, Schmalbein D, Kamlowski A, Water/moisture and fat analysis by time-domain NMR. Food Chem. 96, 436–440 (2006).

27. Apih T, Rameev B, Mozzhukhin G, Barras J, in NATO Advanced Research Workshop on Magnetic Resonance Detection of Explosives and Illicit Materials (Springer, 2012).

28. Tourell MC, Ali TS, Hugo HJ, Pyke C, Yang S, Lloyd T, Thompson EW, Momot KI, T1-based sensing of mammographic density using single-sided portable NMR. Magn. Reson. Med 80, 1243–1251 (2018). [PubMed: 29399874]

29. Gambarota G, Ciarns BE, Berde CB, Mulkern RV, Osmotic effects on the T2 relaxation decay of in vivo muscle. Magn. Reson. Med 46, 592–599 (2001). [PubMed: 11550254]

30. Ababneh Z, Beloeil H, Berde CB, Gambarota G, Maier SE, Mulkern RV, Biexponential parameterization of diffusion and T2 relaxation decay curves in a rat muscle edema model: decay curve components and water compartments. Magn. Reson. Med 54, 524–531 (2005). [PubMed: 16086363]

31. Araujo ECA, Fromes Y, Carlier PG, New insights on human skeletal muscle tissue compartments revealed by in vivo T2 NMR relaxometry. Biophys. J 106, 2267–2274 (2014). [PubMed: 24853755]

32. Fan RH, Does MD, Compartmental Relaxation and diffusion tensor imaging measurements in vivo in λ-carrageenan-induced edema in rat skeletal muscle. NMR Biomed. 21, 566–573 (2008). [PubMed: 18041804]

33. Ho SN, Intracellular water homeostasis and the mammalian cellular osmotic stress response. J. Cell. Physiol 206, 9–15 (2006).CrossRefPubMedWeb of ScienceGoogle Scholar [PubMed: 15965902]

34. Li M, Vassiliou CC, Colucci LA, Cima MJ, 1H nuclear magnetic resonance (NMR) as a tool to measure dehydration in mice. NMR Biomed. 28, 1031–1039 (2015). [PubMed: 26123278]

35. Costill DL, Saltin B, in Metabolic Adaptation to Prolonged Physical Exercise, Howald H, Poortmans JR, Eds. (Birkhäuser, 1975), pp. 352–360.

36. Nose H, Morimoto T, Ogura K, Distribution of water losses among fluid compartments of tissues under thermal dehydration in the rat. Jpn. J. Physiol 33, 1019–1029 (1983). [PubMed: 6674653]

37. Bashyam A, Li M, Cima MJ, Design and Experimental Validation of Unilateral Linear Halbach Magnet Arrays for Single-Sided Magnetic Resonance. J. Magn. Reson 292, 36–43 (2018). [PubMed: 29763794]

38. Freedman R, Heaton N, Fluid Characterization Using Nuclear Magnetic Resonance Logging. Petrophysics 45, 241–250 (2004).

39. Wang J-Z, Mezrich RS, Kostis JB, The use of magnetic resonance imaging in the study of endema. Angiology, 358–364 (1991). [PubMed: 2035887]

40. Meler JD, Solomon MA, Steele JR, Yancy CW Jr.., R. W. Parkey, J. L. Fleckenstein, The MR appearance of volume overload in the lower extremities. J. Comput. Assist. Tomogr 21, 969–973 (1997). [PubMed: 9386292]

41. Shemin D, Dworkin LD, Sodium balance in renal failure. Curr. Opin. Nephrol. Hypertens 6, 128–132 (1997). [PubMed: 9146973]

42. Ronco C, Fluid Overload: Diagnosis and Management (Karger, 2010).

43. Bhave G, Neilson EG, Volume depletion versus dehydration: How understanding the difference can guide therapy. Am. J. Kidney Dis 58, 302–309 (2011). [PubMed: 21705120]

44. Connor S, Nicholson JK, Everett JR, Chemical-exchange and paramagnetic T2 relaxation agents for water suppression in spin-echo proton nuclear magnetic resonance spectroscopy of biological fluids. Anal. Chem 59, 2885–2891 (1987). [PubMed: 3434814]

45. Zuo CS, Villafuerte RA, Henry ME, Butman M, Dobbins RL, He Y, Orban BS, Cayetano K, Wang L, Brown AP, Nunez DJ, Brown J, Renshaw PF, Proton and sodium MRI assessment of fluid level in calf tissue. J. Magn. Reson. Imaging 24, 191–196 (2006). [PubMed: 16758473]

46. Margaret Cheng H-L, Stikov N, Ghugre NR, Wright GA, Practical medical applications of quantitative MR relaxometry. J. Magn. Reson. Imaging 36, 805–824 (2012). [PubMed: 22987758]

47. Yankeelov T, Pickens DR, Price RR, Quantitative MRI in Cancer (CRC Press, ed. 1, 2012).

48. Wood JC, Enriquez C, Ghugre N, Tyzka JM, Carson S, Nelson MD, Coates TD, MRI R2 and R2* mapping accurately estimates hepatic iron concentration in transfusion-dependent thalassemia and sickle cell disease patients. Blood 106, 1460–1465 (2005). [PubMed: 15860670]

49. Blümich B, Perlo J, Casanova F, Mobile single-sided NMR. Prog. Nucl. Magn. Reson. Spectrosc 52, 197–269 (2008).

50. Sarracanie M, LaPierre CD, Salameh N, Waddington DEJ, Witzel T, Rosen MS, Low-cost high-performance MRI. Sci. Rep 5, 15177 (2015). [PubMed: 26469756]

51. Veevaete M, "Applications of Earth's Field NMR to porous systems and polymer gels," thesis, Universität Bremen (2008).

52. Tsai LL, Mair RW, Rosen MS, Patz S, Walsworth RL, An open-access, very-low-field MRI system for posture-dependent 3He human lung imaging. J. Magn. Reson 193, 274–285 (2008). [PubMed: 18550402]

53. Cooley CZ, Stockmann JP, Armstrong BD, Sarracanie M, Lev MH, Rosen MS, Wald LL, Two-dimensional imaging in a lightweight portable MRI scanner without gradient coils. Magn. Reson. Med 73, 872–883 (2015). [PubMed: 24668520]

54. McCarthy P, FSLeyes (2019); doi:10.5281/ZENODO.2630502.

55. Hattori K, Ikemoto Y, Takao W, Ohno S, Harimoto T, Kanazawa S, Oita M, Shibuya K, Kuroda M, Kato H, Hattori K, Development of MRI phantom equivalent to human tissues for 3.0-T MRI. Med. Phys 40, 032303 (2013).

56. HYDRA ECF/ICF (Model 4200) (San Diego, CA, USA).

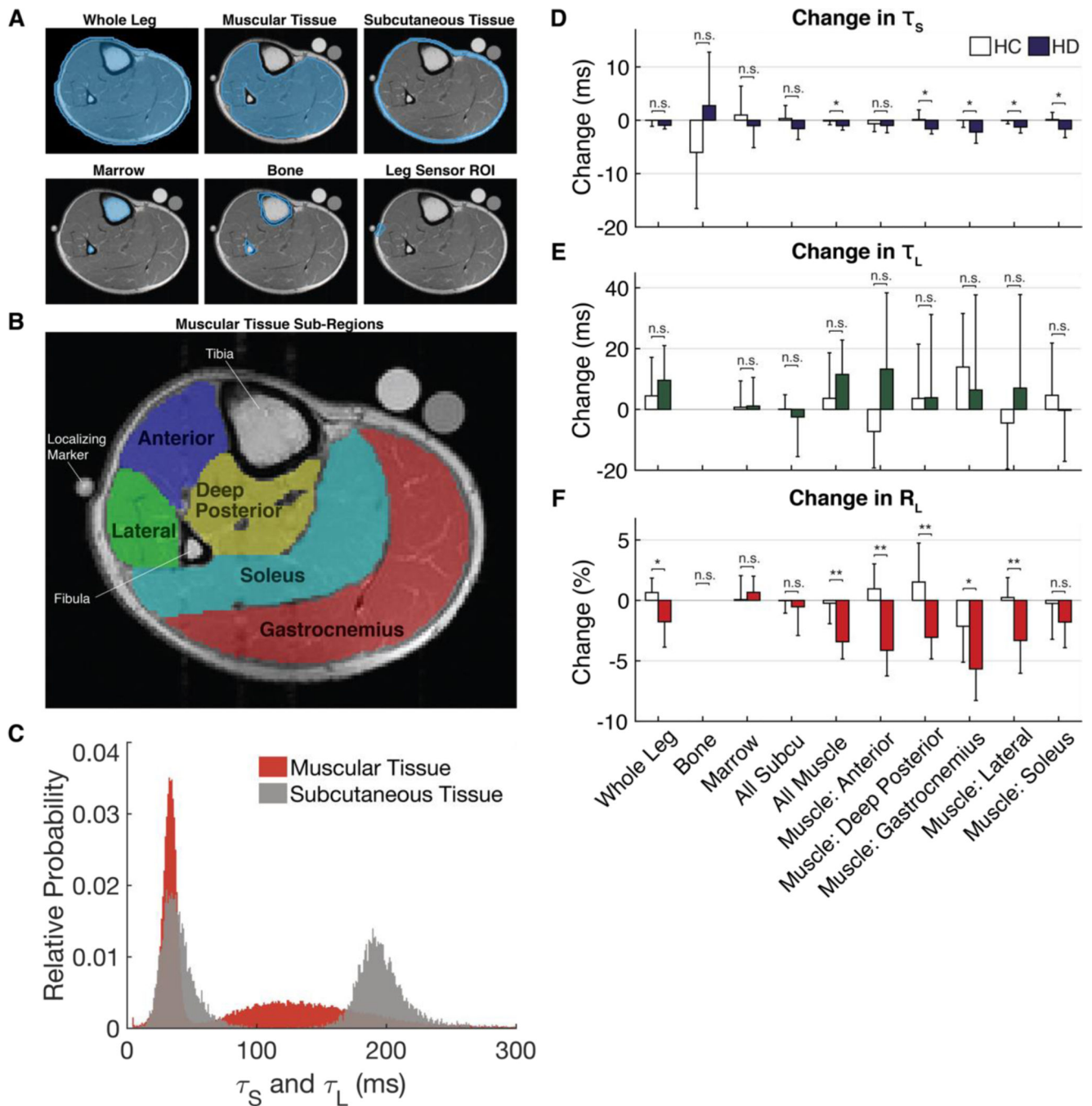57. Feng X, He X, Hu J, Wild bootstrap for quantile regression. Biometrika 98, 995–999 (2011). [PubMed: 23049133]

Figure 1. MRI pixel-wise analysis of changes within ROIs.
(**A**) ROIs were drawn on each slice of each scan for all subjects. Subcutaneous Tissue: includes skin, fat and blood vessels in the fat. Bone and Marrow: include tibia and fibula. Muscular Tissue: includes muscle, fascia, nerves, and blood vessels. Whole Leg: includes all tissues. (**B**) ROIs of sub-muscles were drawn on the first slice of each scan. (**C**) A histogram of the pixel-wise short (T_S) and long (T_L) relaxation values found in the muscular and subcutaneous tissue of a representative subject. The pre-post change in (**D**) T_S, (**E**) T_L, (**F**)

R_L for each ROI across all HC and HD subjects. Bars represent the mean ± SD. ns denotes p 0.05, * for p < 0.05, ** for p < 0.01.
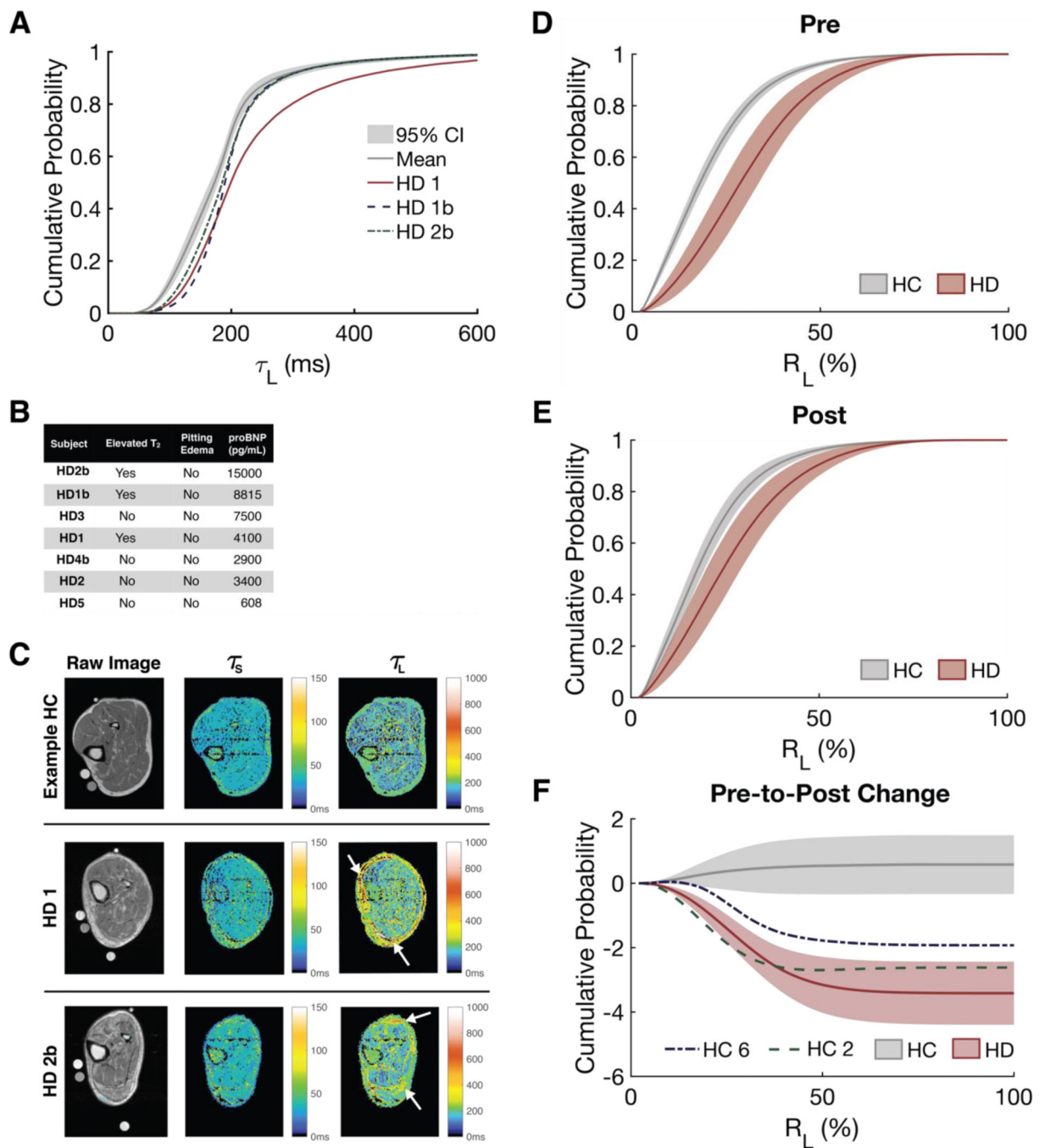
Figure 2. MRI pixel-wise relaxation and relative amplitudes.
(**A**) CDFs of the pixel-wise T_L values found within the entire leg at baseline. The mean and 95% confidence interval (CI) of all subjects is in grey. (**B**) Summary of the proBNP and clinical examination results for HD subjects. (**C**) Heatmaps of T_S and T_L for a sample healthy control, HD1, and HD2b. Perifascial fluid deposits and/or subcutaneous edema are indicated by arrows. Average CDF of the pixel-wise R_L in the muscle for HC and HD subjects (**D**) pre- and (**E**) post-time points. (**F**) The change in R_L for HC and HD subject

groups. HC2 and HC6 not included in HC average for figure 4F. All cdf figures are plotted as mean ± 95% CI.
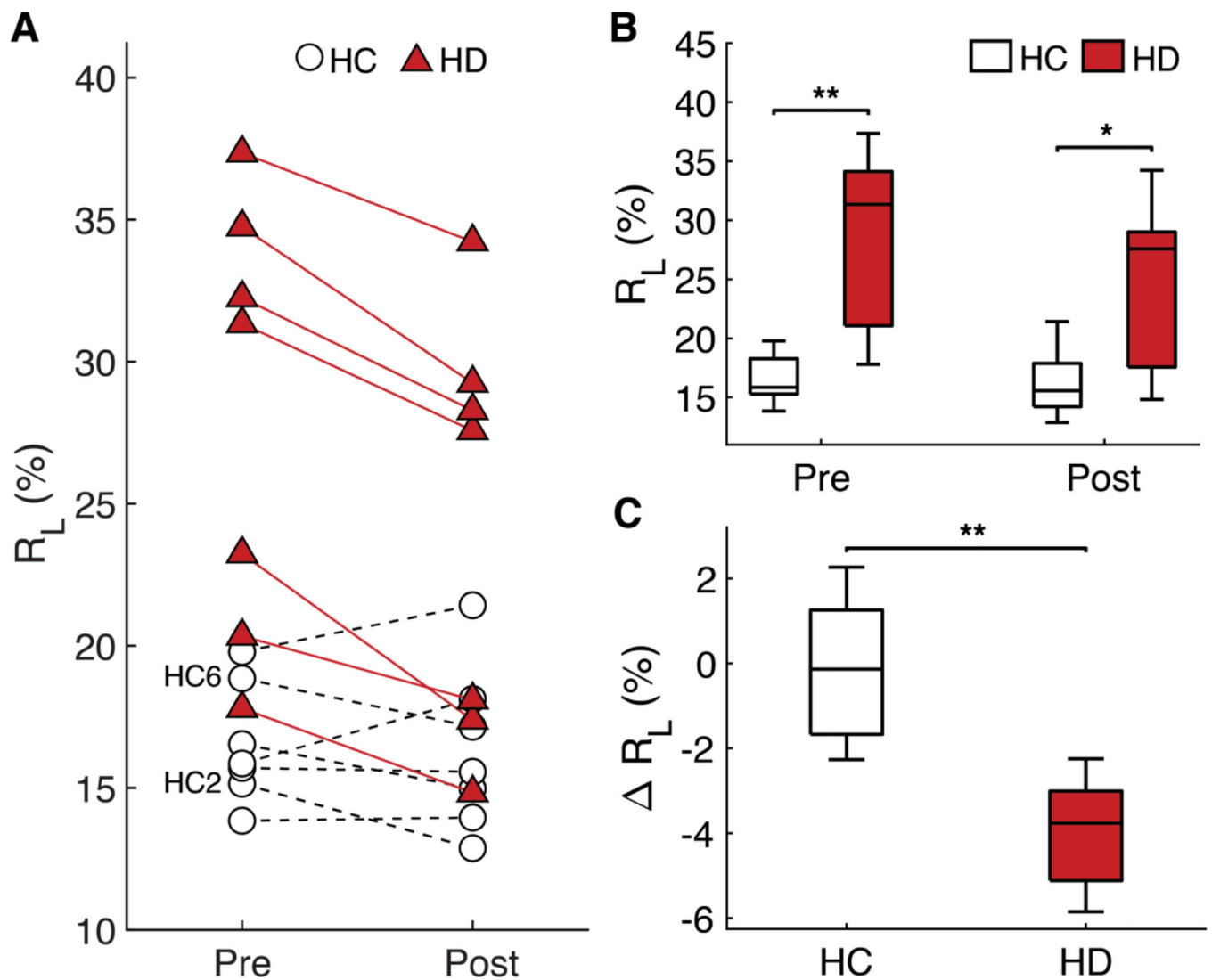
Figure 3. MRI muscle ROI bi-exponential fit results.
(**A**) The R_L values of the muscle ROI for each subject. (**B**) Pre- and post- muscle R_L values of HC and HD groups. (**C**) The change in muscle R_L for HC and HD subjects. The central mark in each boxplot indicates the median, and the bottom and top edges of the box indicate the 25th and 75th percentiles, respectively. The whiskers extend to the most extreme values not considered outliers. * denotes $p < 0.05$, ** denotes $p < 0.01$.
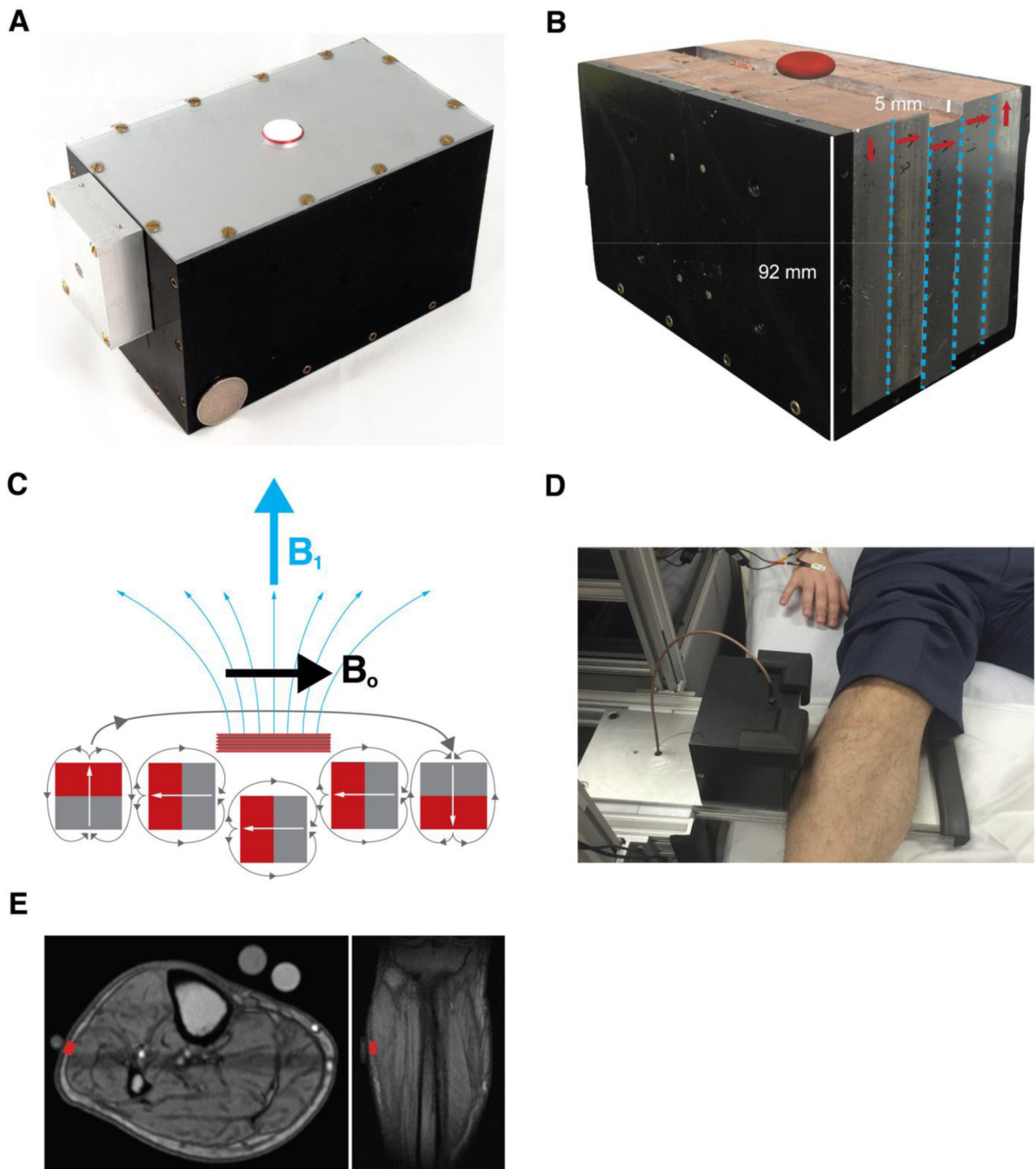
Figure 4. Portable single-voxel NMR sensor for bedside measurements.
(**A**) Photo of the complete NMR sensor, RF coil, and box containing the matching circuitry for the coil. A US Quarter is used for scale. (**B**) Photo of the NMR sensor with the top and side removed. Arrows denote magnetic orientation of each slab. Red ellipsoid above sensor denotes approximate sensor measurement region. (**C**) Schematic of linear Halbach design showing magnetization orientation of the individual magnets as well as the net B_o and B_1 orientations. (**D**) Photo of the NMR sensor in use at the hospital for bedside assessment. (**E**)

Sagittal and transverse MRI scans showing the location of the NMR sensor's approximately measurement voxel in red.
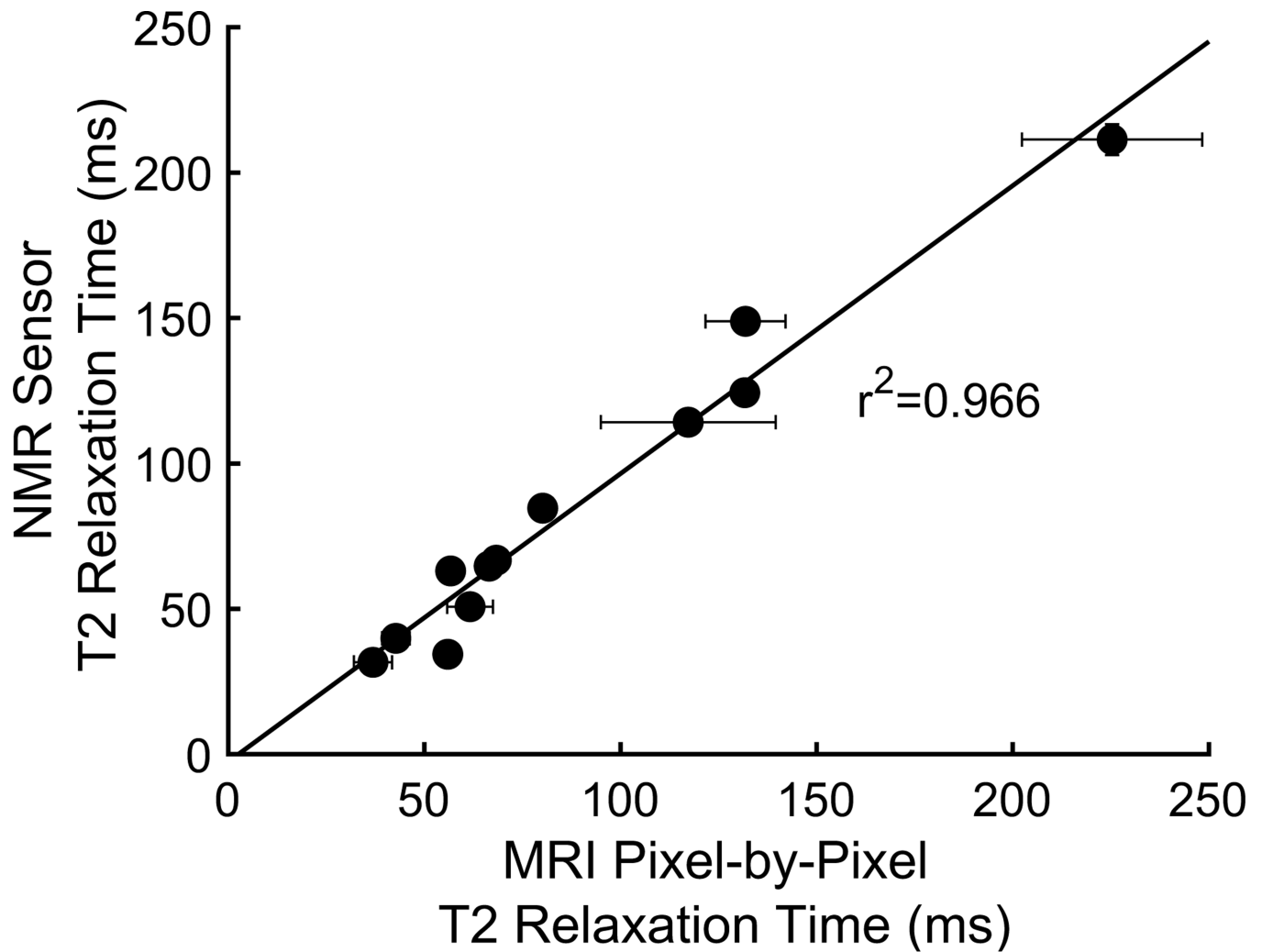
Figure 5. Comparison of T2 relaxation times from MRI pixel-by-pixel and NMR sensor.
Both mono- and bi-exponential fit results of each of the six phantoms and ex-vivo tissue
samples. There is a strong correlation between the MRI and NMR sensor values (r^2=0.966)
suggesting that the results can be translated between the two sensors. Vertical (NMR sensor)
error bars represent the 95% confidence interval for the fit. Horizontal (MRI) error bars
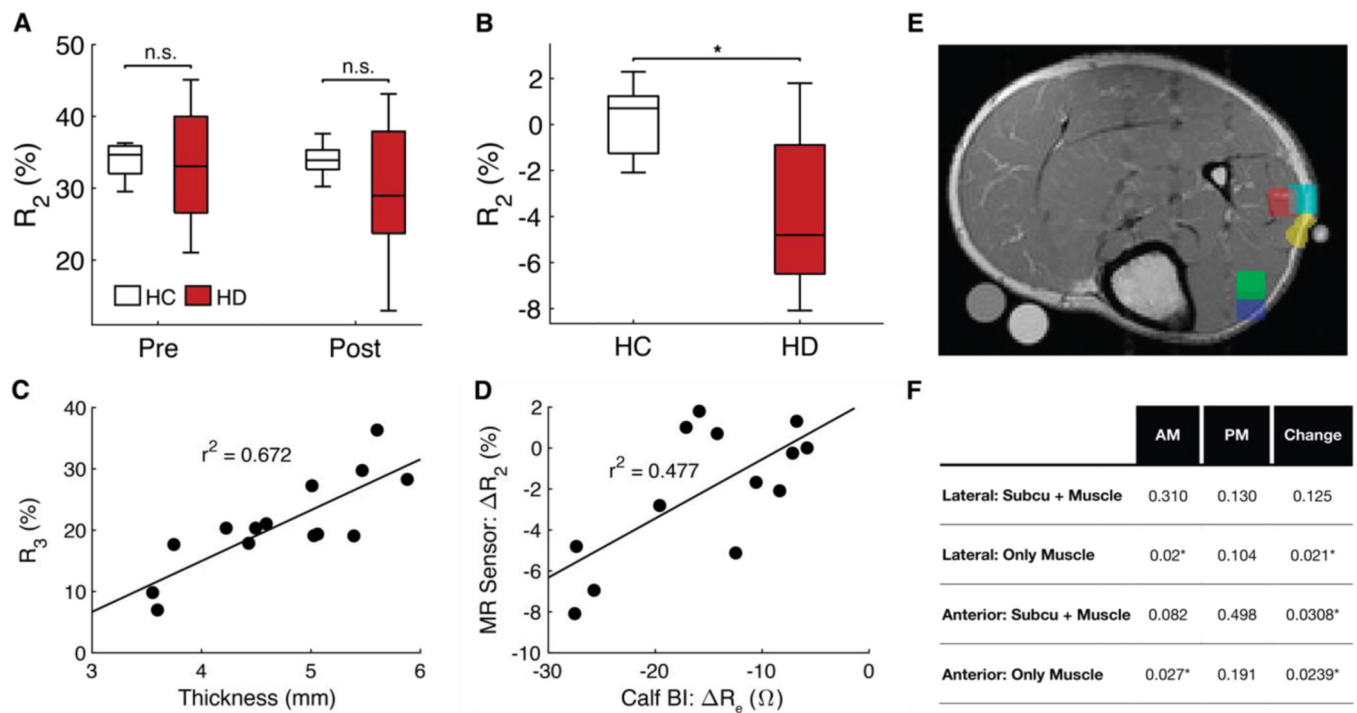represent the standard deviation of the pixel-by-pixel MRI results.

Figure 6. NMR sensor results and future design criteria.

(**A**) Boxplots displaying R_2 values at pre- and post- time points, and (**B**) the change in R_2 for HC and HD subjects. The central mark in each box plot indicates the median, and the bottom and top edges of the box indicate the 25th and 75th percentiles, respectively. The whiskers extend to the most extreme values not considered outliers. (**C**) R_3 plotted against subcutaneous tissue thickness ($r^2=0.672$). Note that the tissue thickness is compressed by a few millimeter when the leg is pressed against the NMR sensor for measurements. (**D**) Change in R_2 plotted against calf bioimpedance's change in ECF-associated resistivity, R_e ($r^2=0.477$). (**E**) MRI scan showing the size and location of some of the smaller ROIs. (**F**) Summary of P values comparing HC and HD subjects for each small ROI (detailed statistics in tables S19-S22). P-values are calculated by a two-sample permutation test with Monte Carlo estimation using 10^5-1 repetitions. * signifies $p < 0.05$.
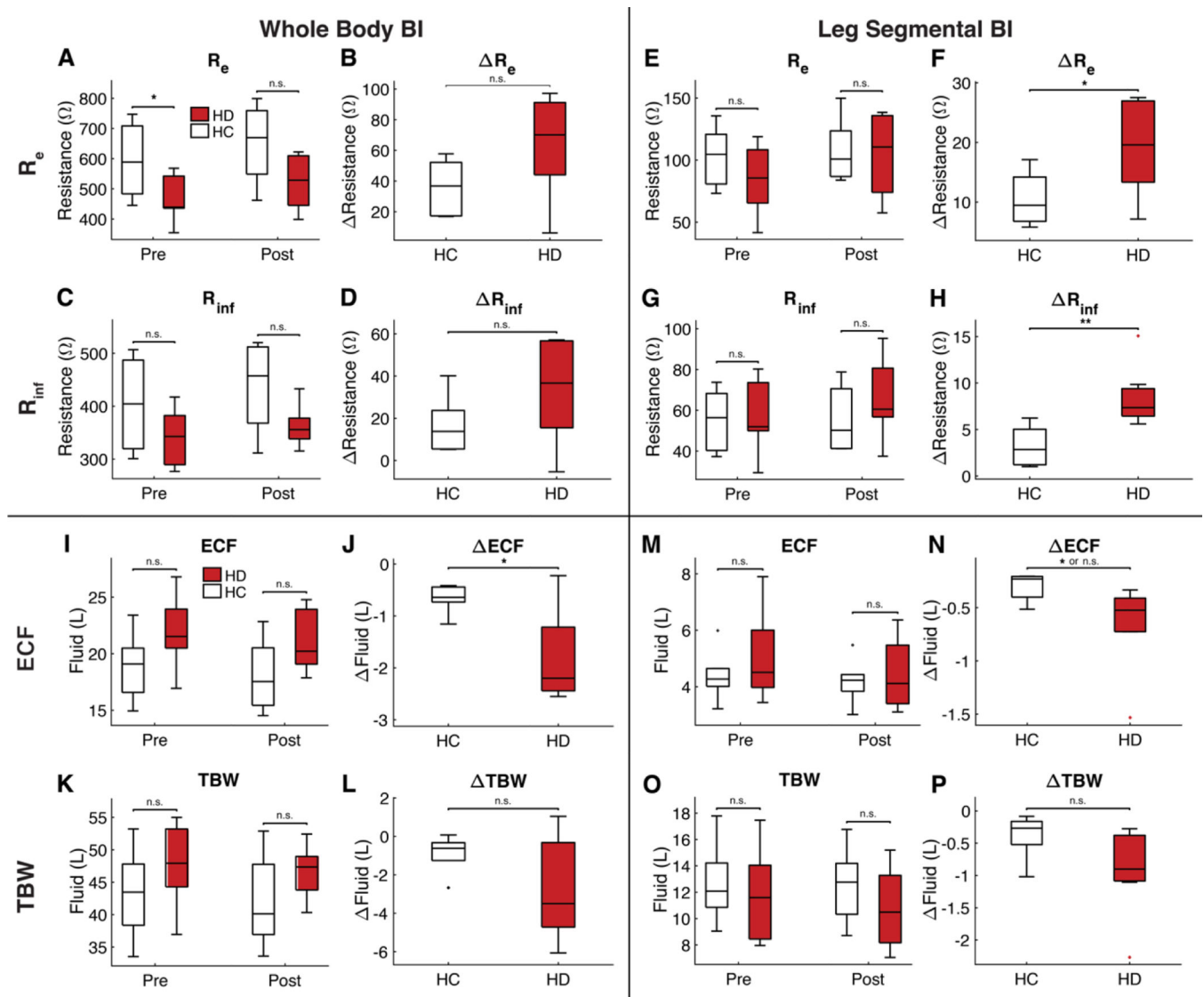
Figure 7. Bioimpedance Comparison of HC and HD Subjects.
Panels (**A**)-(**H**) represent raw resistivity measurements whereas (**I**)-(**P**) represent TBW and ECF bioimpedance measurements. Panels (**A**)-(**D**) come from whole body bioimpedance measurements whereas panels (**E**)-(**H**) come from segmental leg bioimpedance measurements. The top row of panels shows R_e data, which corresponds to ECF. The second row of panels shows R_{inf} data, which corresponds to TBW. Fluid has a low resistivity. Low resistivity indicates more fluid. Higher resistivity indicates less fluid. An increase in resistivity indicates decrease of fluid. It is only possible to distinguish HD from HC subjects at a single time point with a whole body R_e measurement at baseline (**A**). Panels (**F,H**) show that it is possible to distinguish HD from HC subjects based on the change in R_e and R_{inf} in the leg. Panels (**I**)-(**L**) come from whole body bioimpedance measurements whereas panels (**M**)-(**P**) come from segmental leg bioimpedance measurements. The third row of panels shows ECF data. The bottom row of panels shows TBW data. It is only possible to significantly distinguish HC from HD subjects based on the change in whole-body

(p=0.027) or leg (p=0.014 with permutation test; p=0.054 with Welch test) ECF. n.s. indicates p>0.05, * indicates p<0.05, ** indicates p<0.01.
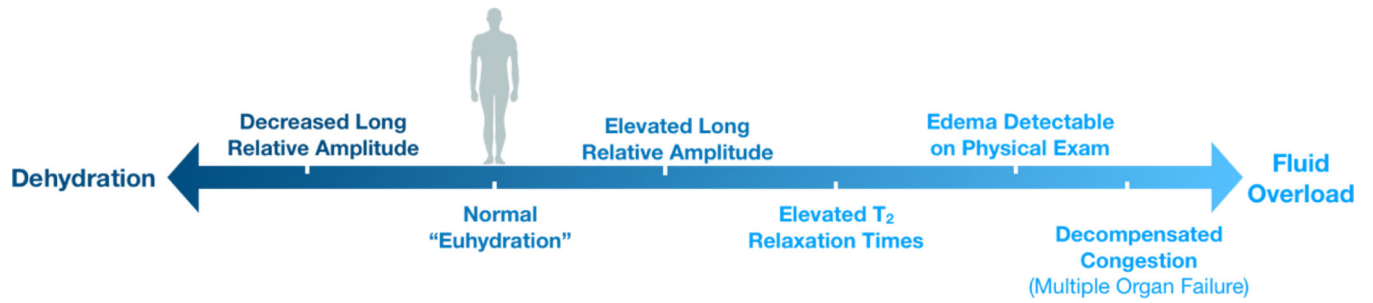
Figure 8. MR relaxometry findings at different fluid states.
Graphical summary of the relaxometry findings – through both traditional MRI and portable NMR sensor – at different clinical fluid states. All findings were observed in the muscular tissue.

Table 1.

Demographics summary of study cohort.

ESRD patients treated with hemodialysis (HDs) and age-matched healthy controls (HCs) were recruited for the study. 1 HC subject and 2 HD subjects completed the study twice. Reported blood value results are from baseline blood draws. Fluid loss is determined based on weight change as a percentage of baseline weight. Values represent Mean ± Standard Deviation.

		Healthy Controls (HC)	Hemodialysis Subjects (HD)
n	#	7 (6 unique)	7 (5 unique)
Age	yrs	54.2 ± 4.9	55.1 ± 10.3
% White		85.7%	42.9%
BMI	kg/m^2	25.1 ± 4.4	27.8 ± 5.0
Fluid Loss	kg	0.6 ± 0.2	2.2 ± 1.2
Fluid Loss	%	0.7 ± 0.3	2.6 ± 1.4
HD vintage	days	NA	1013 ± 699.8
Sodium	mmol/L	140.6 ± 2.1	139.1 ± 1.6
BUN	mg/dL	16.0 ± 4.4	58.1 ± 14.5
Creatinine	mg/dL	0.8 ± 0.2	8.3 ± 1.8
WBC	x10e3/uL	5.0 ± 1.6	7.6 ± 1.1
Platelets	x10e3/uL	255.3 ± 77.1	184.3 ± 87.4
Osmolality	mOsm/kg	291.6 ± 5.8	307.7 ± 4.1
BNP	pg/mL	18.4 ± 5.4	6086.1 ± 4495.9